

Organic and Inorganic Scintillation Detector Calibration and Optimization for Neutral Atom
Trap for Beta Decay

Summer 2022 CO-OP Work Term Report

Melisa Ozen

University of Ottawa

Abstract

At TRIUMF's Neutral Atom Trap for Beta Decay, we investigate the time-reversal symmetry in beta decays of trapped atoms. For a four-momentum state, such as during a radiative beta decay when a gamma is also emitted, the correlation of the three momenta from beta-neutrino-gamma coincidences could indicate a violation of the time-reversal symmetry. Such a study requires high precision measurements in energy regions higher than 511 keV. Here, we report the calibration and optimization studies for a plastic and two GAGG (Gadolinium Aluminium Gallium Garnet) scintillation detectors with Si photomultiplier (SiPM) readouts for the detection of decay products and gamma emissions. We implemented a known differentiation method to approximate the location of Compton edges from gamma-ray emissions for the plastic detector while a combination of Gaussian and error functions was adopted to calibrate the GAGG detectors. Convolutions of GEANT4 simulations were used for resolution estimations for gamma-ray emissions while the energy resolution was determined to be 10-11% for internal conversion electrons around 1 MeV for the plastic scintillator. Several reflectors used for wrapping the scintillators including PTFE, ESR (enhanced specular reflector) and nitrocellulose were compared in terms of the change in the detector resolutions. The effect of the increasing overvoltage bias on the photon detection efficiency and dark currents was also studied for both types of detectors. Furthermore, we attenuated the pulse signals, modified the printed circuit board used for the SiPM readouts and swapped the two scintillators to investigate the difference in energy resolutions between the two GAGG detectors and traced it to the intrinsic differences between the two scintillator crystals. The average energy resolutions for GAGG detectors were determined as 8.9% and 6.9% at 662 and 1333 keV gamma-ray photopeaks, respectively. The gamma-ray coincidences between the two GAGG detectors were also investigated, and a coincidence timing resolution of 6.1 ± 0.5 ns was determined.

Keywords: radiation detection, scintillation detectors, gamma rays, time-reversal symmetry

Table of Contents

1	Introduction	3
2	Background Theory	3
3	High Energy Radiation Detection with Scintillation Detectors.....	3
3.1	Scintillation Mechanism.....	3
3.2	Organic Scintillation Detectors	4
3.2.1	Experimental Setup.....	4
3.2.2	Detector Calibrations	6
3.2.3	Optimization Studies.....	7
3.3	Inorganic Scintillation Detectors.....	9
3.3.1	Experimental Setup.....	9
3.3.2	Detector Calibrations	11
3.3.3	Optimization Studies.....	12
3.3.4	Coincidence Timing Resolution	16
4	Future Perspectives.....	17
5	Conclusion.....	18
	References.....	18

1 Introduction

Time-reversal symmetry breaking in weak interactions could indicate physics beyond the Standard Model. We require high-precision methods to observe the correlation of three momenta that could suggest a symmetry violation, such as the beta-neutrino-gamma coincidences during a radiative beta decay [1]. Scintillation detectors have been used for the longest time to detect ionizing radiation [2]. In this report, we present our calibration and optimization studies for organic and inorganic scintillators for detecting the decay products of trapped atoms.

The first part of this report focuses on the background theory of the time-reversal symmetry violations which is the main motivation for this research. The scintillation mechanism for both the organic and inorganic scintillation detectors was also explained. In the second part, we explained a useful differentiation method for the estimation of the Compton edge locations for calibrating an organic scintillation detector using gamma-ray sources. We also used a Monte Carlo simulation software called GEANT4 to simulate the Compton edges from the gamma-ray emissions and then to estimate the energy resolution. The effect of the overvoltage bias on the energy resolution was reported for the organic scintillation detector.

Similarly, various optimization studies including overvoltage bias, use of a different reflector material, a Si photomultiplier (SiPM) change, signal attenuation, printed circuit board (PCB) modification, and scintillator crystal swap were discussed for the inorganic Gadolinium Aluminium Gallium Garnet (GAGG) detectors in terms of the change in the energy resolution in the third part of the report. The coincidence timing resolution between the GAGG detectors was also explored.

2 Background Theory

The violation of time-reversal symmetry could indicate physics beyond the electroweak interaction predictions of the Standard Model. We investigate the interactions between the decay products in a radiative beta decay through observing their momenta. A scalar triple product of momenta $p_1 \cdot p_2 \times p_3$ flips sign with the sign of time [1]. A non-zero value of the scalar triple product would indicate a violation of the time-reversal symmetry; however, it is prevented by momentum conservation. The construction of a three-momenta state from a four-momentum final state could resolve this problem. Therefore, we look for $p_\beta \cdot p_\nu \times p_\gamma$ correlation for the radiative beta decay (from the four-momentum final state of $p_{recoil}, p_\beta, p_\nu, p_\gamma$) to investigate the time-reversal symmetry breaking in trapped atoms [1].

3 High Energy Radiation Detection with Scintillation Detectors

3.1 Scintillation Mechanism

Scintillation detectors are used to detect high-energy radiation such as X- and gamma rays. They are composed of scintillators that absorb ionizing radiation and emit lower energy photons [3]. The low-energy light pulses in the visible range are detected by light sensors such as silicon photomultipliers (SiPMs) and photomultiplier tubes (PMTs). Scintillators are luminescent

materials (such as NaI and CsI) that convert a large fraction of the incident radiation energy into prompt fluorescence [2]. They are divided into two categories: organic and inorganic scintillators which have different scintillation mechanisms.

For organic scintillators, the fluorescence process is based on the transitions in the energy levels of the molecules. Energy absorbed from the high-energy photons excites the electron configuration of the molecules into excited singlet (or triplet) states labeled as S_n . The main scintillation occurs when the population of the excited molecules in the S_{10} state transition to the ground electronic state [2].

For inorganic scintillators, the scintillation mechanism is based on the crystal lattice structure. High-energy photons reaching the scintillator create many energetic secondary electrons by exciting the electrons from the valence band to the conduction band [2,3]. These excited electrons interact with the crystal lattice and the other electrons. Luminescence occurs when electrons recombine with holes (which is the case for semiconductor-based scintillators). However, the recombination of electron-hole pairs in semiconductors usually emits photons that are not in the visible range due to band gap structure of semiconductors. Therefore, impurities called activators (such as Ce) are added to the crystals that modify their lattice and the energy structure [2]. In such crystals, luminescent ions are excited by the energetic secondary ions [3].

Organic scintillators are low cost and easy to produce and shape compared to the inorganic ones. However, they are made of low- Z (where Z is the effective atomic number) and low-density materials like plastic and polyester which makes them ineffective for gamma-ray detection. Therefore, they are usually preferred for beta spectroscopy while inorganic crystals are used for gamma-ray spectroscopy [2, 4]. Moreover, scattering of the beta particles from materials as well as the bremsstrahlung photons emitted from the beta particles scale with Z . Therefore, in low- Z organic scintillators, electrons have a higher probability of depositing their full energies.

3.2 Organic Scintillation Detectors

3.2.1 Experimental Setup

The scintillation detector assembly is described in Fig. 1. The organic scintillator used for the radiation detection experiments was a plastic scintillator with a 90 mm diameter and a 35 mm thickness. It is crucial to use a good reflector to minimize the light loss from the sides of the scintillator. The PTFE tape is reported to have a high reflection rate, up to 96.2% for 8 layers at 440 nm and the reflectivity increases with the increasing number of layers. For at least 95% reflectivity, the required thickness of PTFE tape would be 0.5 mm [5]. Therefore, we wrapped the scintillator with 4 layers of PTFE tape (i.e., Teflon) except for the top and bottom parts. One layer of ESR (enhanced specular reflector) with a thickness of 0.075 mm was placed on the top of the scintillator and the bottom part was left unwrapped to allow the scintillation light to reach the readout. The scintillator was then coupled with an 8x8 array of SensL ArrayJ-60035-64P 6mm SiPMs. We placed a thin layer of gel between the SiPM array and the scintillator surface to minimize the light losses between the scintillator and SiPM window mediums due to the difference in refractive indexes compared to air.

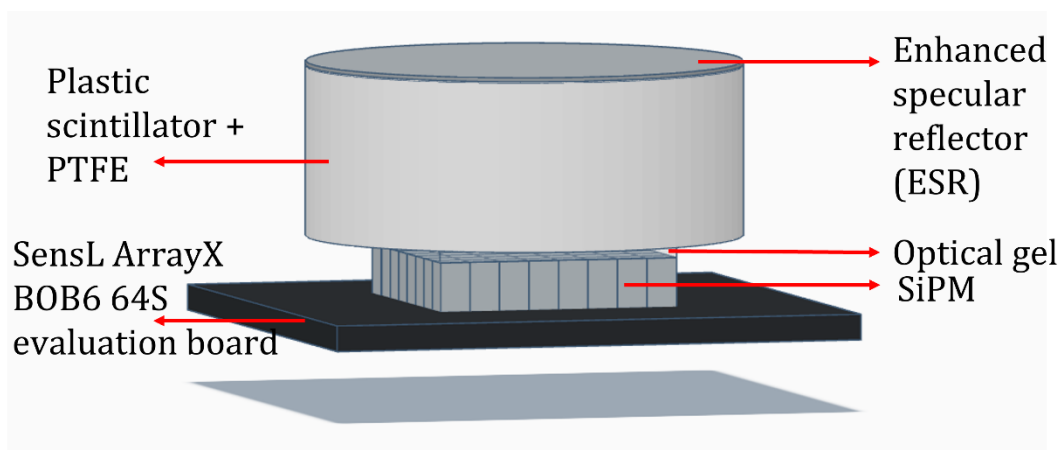


Fig. 1. Plastic scintillation detector assembly. The scintillator was wrapped with 4 layers of PTFE tape around the sides and with one layer of ESR film on top. The SiPM used

SiPMs are composed of thousands of microcells, each containing a single photon avalanche diode (SPAD). When a photon reaches Si, which is a semiconductor, it creates an electron-hole pair in the depletion region. Reverse biasing diodes creates an electric field in the depletion region which accelerates the charge carriers. When sufficient reverse bias is applied, the charge carriers create secondary charge pairs and cause the Si to become conductive. This is called the breakdown voltage and a typical value for SiPMs is 24 V [6]. SiPM sensors were used for the pulse readout as they are insensitive to magnetic fields, unlike PMTs. The gain for PMTs changes with the varying direction and strength of the magnetic field which is not ideal for the radiation detection calibrations for our magneto-optical atom trap. SiPMs are also compact, do not require very high voltages to operate (around 25-30 V) and have high photon detection efficiency (PDE).

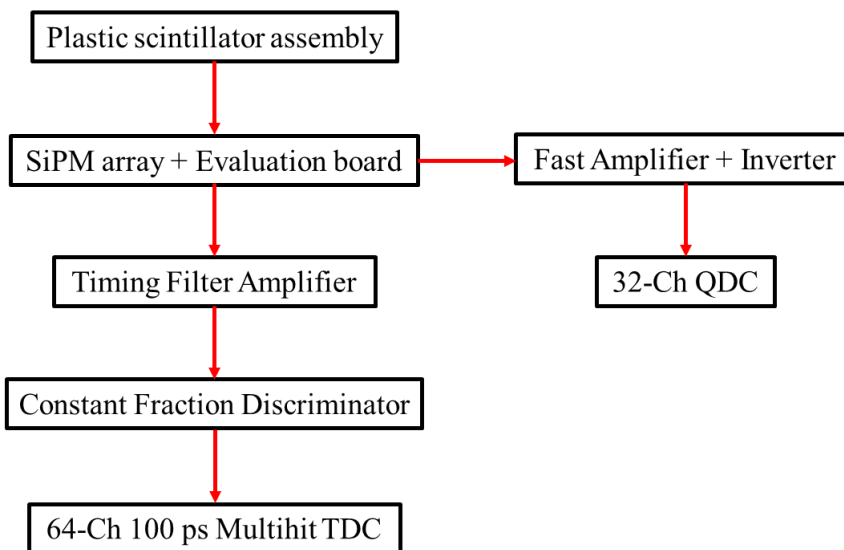


Fig. 2. Schematic diagram of the data acquisition system for the plastic scintillation detector.

The data acquisition system for the plastic detector is described in Fig. 2. We coupled our SiPMs with a SensL ArrayX BOB6 64S evaluation board for the readout. The signal output was connected across an Ortec 454 1 kOhm timing filter amplifier (TFA) for pulse shaping and the

optimization of the signal-to-noise ratio. The signal was then tuned by a RoentDek Constant Fraction Discriminator (CFD) which is used to improve the time response of electronic signals from secondary emission devices like photomultipliers and multichannel plates [7]. The output of the CFD was read by a 64-Channel 100 ps Multihit Time to Digital Converter (TDC) by CAEN. The output signal was also amplified by a Roentdek FAMP8 fast amplifier. The polarity of the output signal from the fast amplifier was inverted by an inverter for the QDC that takes negative signals. The output signal from the fast amplifier and the inverter was connected to a 32-Channel charge-to-digital converter (QDC) by CAEN for data acquisition. ROOT software developed by CERN for high-energy physics was used to collect the QDC histograms from the scintillation detector.

3.2.2 Detector Calibrations

To calibrate the gain of our detector for the 0.5 – 3 MeV energy range, which is the energy region of interest for our radiative beta decay experiments, we used radioactive isotopes that emit gamma rays. When an incident gamma ray scatters off the scintillator and escapes, it collides with an electron. During this process, called the Compton scattering, some amount of energy is exchanged between the gamma ray and the electron. This energy varies with an angle and is at maximum when the incident gamma ray is scattered through 180° . This energy is called the Compton edge and can be calculated through [8]:

$$E_c = \frac{2E^2}{m_e c^2 + 2E}$$

Where E_c is the Compton energy, E is the energy of the incident photon, m_e is the mass of the electron, c is the speed of light, and $m_e c^2 = 0.511$ MeV.

Low-Z plastic scintillators like ours are not usually used for gamma ray detection since they cannot detect gamma ray photopeaks. However, Compton edges for gamma-ray sources can be observed in plastic scintillation detectors. Therefore, we used a differentiation method introduced by Safari *et al.* to estimate the location of Compton edges from gamma-ray emissions [9]. This method proposes that an ideal Compton edge can be described by a second-order step function. This function is convolved into a Gaussian function to take detector resolution into account. However, with increasing σ (related to detector resolution), the local maximum shifts from the actual value of the Compton edge. Therefore, taking the half-value of the local maximum of this convolved function cannot be considered a reliable method to estimate the Compton energy. The group suggests that, when differentiated, the local minimum of the convolved function corresponds to the Compton edge, expressed as [9]:

$$R'(E) = X_1(E) + X_2(E) \quad (1)$$

Where R' is the differentiated detector response function,

$$X_1(E) = \alpha \cdot \operatorname{erfc}\left(\frac{E-E_c}{\sqrt{2}\sigma}\right) \quad (2)$$

$$X_2(E) = \beta \cdot \exp\left(-\frac{(E-E_c)^2}{2\sigma^2}\right)$$

Where $\operatorname{erfc}(E)$ is the complementary error function and,

$$\alpha \equiv \frac{1}{2}(2aE + b) \quad (3)$$

$$\beta \equiv -\frac{1}{\sqrt{2\pi}\sigma} [a(E_c^2 + 2\sigma^2) + bE_c + c]$$

Therefore, we used this differentiation method to locate the Compton energies on the energy spectra we collected from the gamma-ray sources: ^{137}Cs , ^{207}Bi and the background sources such as ^{40}K and ^{208}Tl . Having multiple radioactive sources is useful for determining the offset and the gain for the detector. On Python, we implemented the non-linear least squares regression model to the differentiated response function in Eq. 1 (Fig. 3). The energy gain for the SiPM readouts is linear, therefore we only needed to find the corresponding channel numbers on ROOT to the known Compton energies of the various gamma-ray sources. This allowed us to calibrate our plastic scintillation detector.

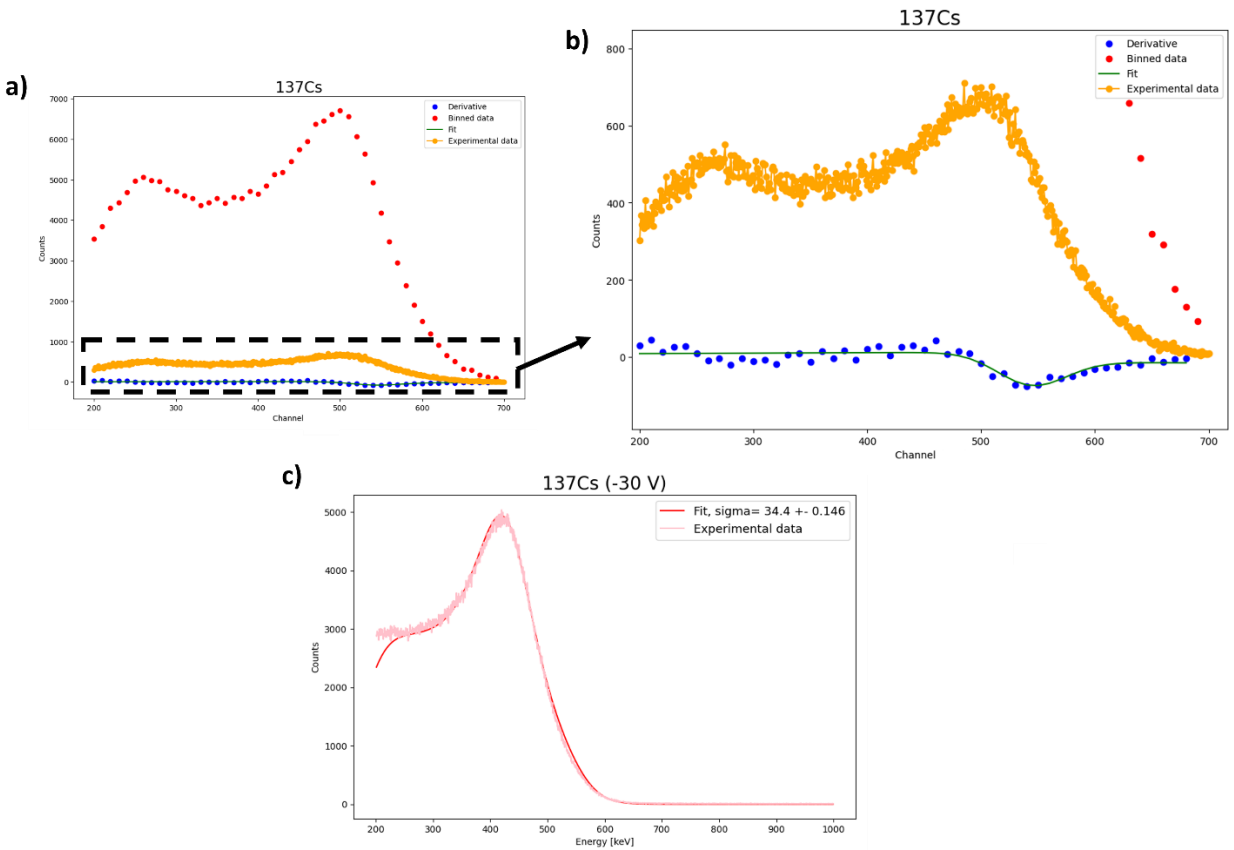


Fig. 3. The differentiation method used to estimate the location of the Compton edge of ^{137}Cs for the plastic scintillation detector. **(a)** and **(b)** show the differentiated response function R' fitted to do the derivative of the detector output. **(c)** depicts the GEANT4 simulation convolved with a Gaussian function and fitted to the experimental output of the detector.

3.2.3 Optimization Studies

Usually, SiPMs operate at a few voltages higher than the breakout voltage (24.5 V for our SiPMs) which is called the overvoltage. Quantum efficiency (QE) is defined as the probability of an incident photon creating an electron-hole pair in the sensor and photon detection efficiency is a measure of the sensitivity of a SiPM [6]. The two are usually used similarly to define the

performance of a SiPM. PDE is affected by the incident photon wavelength, the applied overvoltage and the microcell fill factor. The manufacturing company of our SiPMs, SensL by Onsemi, reports 45% of photon detection efficiency (PDE) at 30 V of applied bias voltage and an overall increase in PDE with an increasing bias voltage. However, they also report a rise in the dark current and crosstalk at higher bias voltages [6]. Therefore, the bias voltage of the SiPMs should be optimized for the best results.

Energy resolution (ΔE) of a detector is determined through $FWHM/E$ where E represents the energy of a photo absorption peak in an energy spectrum, $FWHM = 2.355\sigma$, and σ is the standard deviation in a normal (i.e., Gaussian) distribution [3]. To be able to evaluate the energy resolution change with the overvoltage, we simulated the Compton scattering for our plastic scintillator through a Monte Carlo simulation software called GEANT4. We convolved the simulations with Gaussian distributions to consider the detector resolution and fit it into our experimental outputs to estimate the energy resolution at three different bias voltages, as shown in Fig. 3c. Our SensL evaluation board operates by negative polarity bias voltage, therefore we negatively biased our SiPMs.

Figure 4 reveals the ΔE change at different energies with increasing negative bias voltage. Due to the nature of the calibrations, our data points had significant uncertainties. This makes it harder to distinguish the energy resolution differences between -28.2 V and -30 V and we see alternating results at different energies. However, we determined that often with raising bias voltage, ΔE decreases. This change is more apparent at bias voltages higher than -26.5 V. Therefore, we achieve better energy resolution due to increasing PDE.

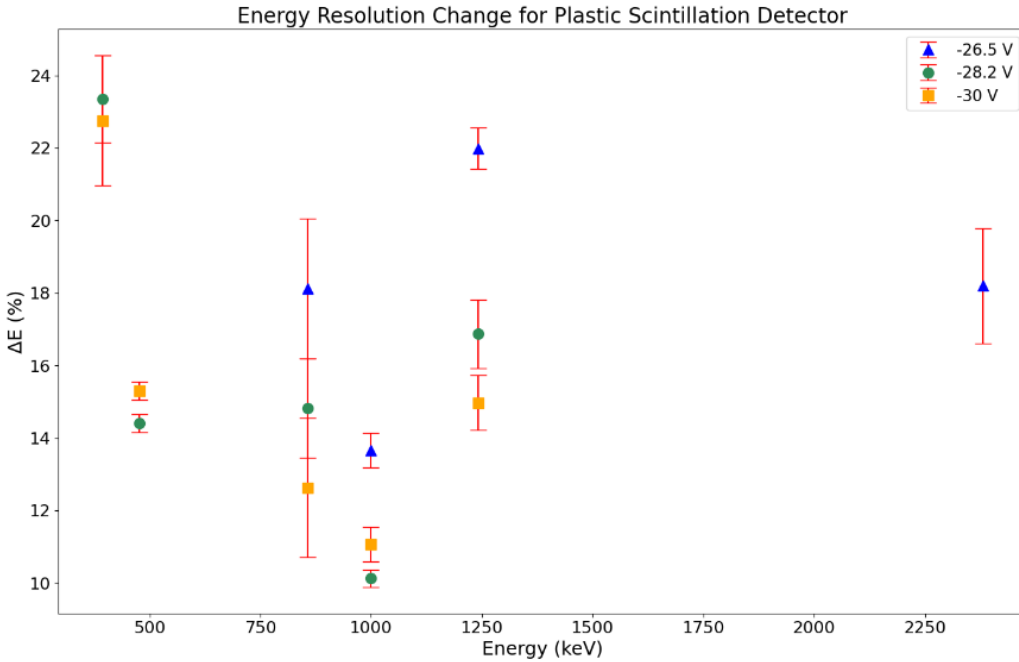


Fig. 4. Change in energy resolution of the plastic scintillation detector with the increasing bias voltage.

However, these energy resolution estimations were determined for gamma-ray sources. As mentioned above, this plastic scintillator is a low-Z material and our detector is designed to detect beta particles, not gamma rays. Therefore, we decided to determine the energy resolution according to internal conversion (IC) electrons. During internal conversion for high-Z isotopes like ^{207}Bi , one of our radioactive sources, the high energy radiation from the decaying isotope interacts with an electron from the outer shells instead of radiating a gamma ray, causing the electron to be ejected from the atom [10]. These electrons can be detected by the organic scintillation detectors as energetic peaks.

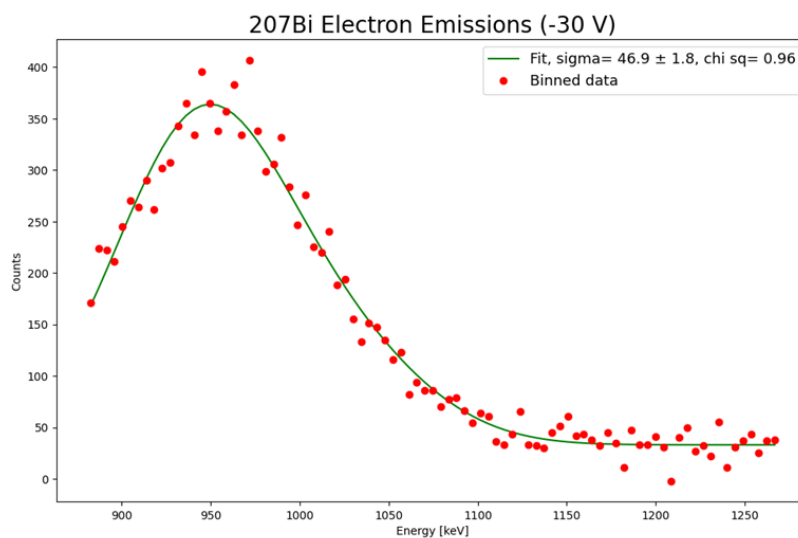


Fig. 5. Gaussian (normal) distribution fitted to the energetic peak of the IC electrons from the K, L, and M shells of ^{207}Bi .

For ^{207}Bi , the main IC electrons are around 1 MeV for K, L, and M shells, at 975.7, 1047.8, and 1059.8 keV, with 7.1, 1.8, and 0.44% probability, respectively. However, the Compton energy of one of the main gamma-ray emissions for this isotope is 857.7 keV. Therefore, to be able to differentiate the IC electron peak from the Compton edge, we placed a 3.2 mm thick glass piece between the ^{207}Bi source and the plastic detector to block the emitted betas. Then we subtracted this data from the data collected with an unblocked source to get rid of the gamma-ray Compton edges. As a result, we could observe the IC electron peak from the K, L, and M shells combined at around 1 MeV. We fitted a Gaussian model to the experimental data and determined the energy resolution to be 10-11% for the plastic scintillator (Fig. 5).

3.3 Inorganic Scintillation Detectors

3.3.1 Experimental Setup

For gamma-ray emissions, we used two inorganic Gadolinium Aluminium Gallium Garnet (GAGG) detectors doped with Ce, manufactured by Epic Crystal. GAGG ($\text{Gd}_3\text{Al}_2\text{Ga}_3\text{O}_{12}$) is a high-Z scintillator crystal. This crystal was picked for gamma-ray detection due to its high photon yield and peak emission at around 540 nm which makes it suitable for coupling with SiPMs [11]. The GAGG detector assembly is described in Fig. 6. Similar to our plastic detector, we wrapped

it with 3 layers of PTFE and also added one layer of ESR to further minimize the light losses from the sides of the scintillator. Circular PTFE caps were placed on the bottom and top parts of the scintillator for the same purpose. At the top part (the readout side), we also placed an optical gel on the scintillator surface just as we did for the plastic detector. The scintillator was coupled with 6 pieces of 2x2 SensL ARRAYJ-60035-4P-PCB 6 mm SiPMs. The detector was placed inside a $\text{\O}3''$ Thorlabs lens tube. The crystal was immobilized inside the tube through a plastic O-ring and sealed with a cap and black tape to ensure a dark condition for the SiPM arrays.

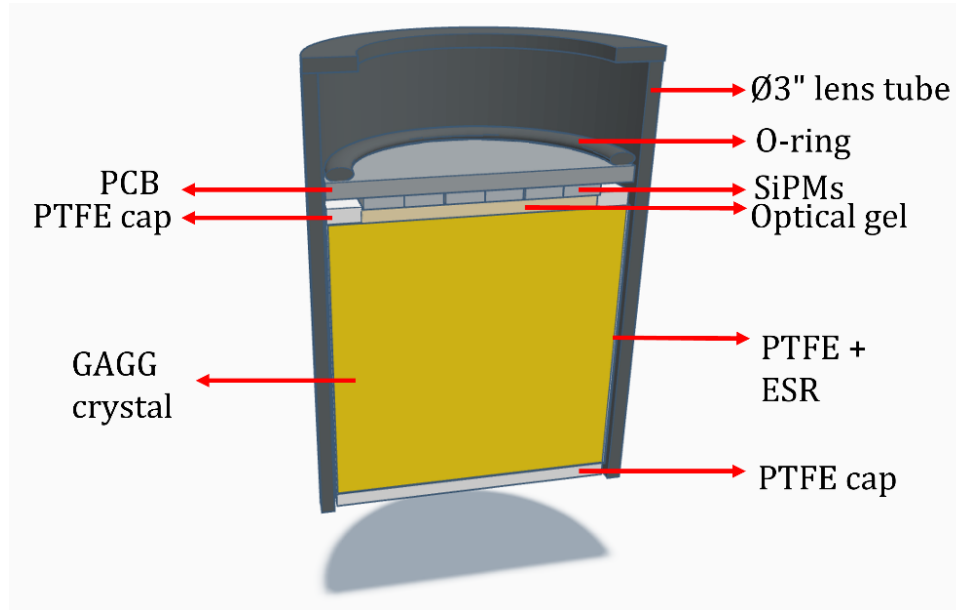


Fig. 6. GAGG detector assembly. The assembly is the same for both detectors. PTFE + ESR represents a single layer of ESR on top of 2-3 layers of PTFE wrapped around the GAGG crystal.

The SiPM signal was read by a printed circuit board (PCB) designed by a previous CO-OP student, Michelle Khoo. The PCB allows the summing of the SiPM currents in two outputs: Slow and Fast outputs in 4 channels each for energy and timing readouts through discharge capacitors with different values (Fig. 7). We used the Slow channels to read the output. The 4 Slow channels were connected to a LeCroy Model 428F Quad Linear Fan-In/Fan-Out with 4 direct-coupled linear inputs and outputs which allowed the summing and polarity inversion of the SiPM signals. One output from the Fan-In/Fan-Out was connected to a 32-Channel QDC through a 50 Ohm splitter and 50 Ohm attenuator. The other output was connected to a LeCroy Model 612AM 6-Channel Variable Amplifier. The amplified signal was then tuned by the same Roentdek CFD that was used for the plastic detector. The output of the CFD was read by a 64-Channel 100 ps Multihit Time to Digital Converter (TDC) by CAEN.

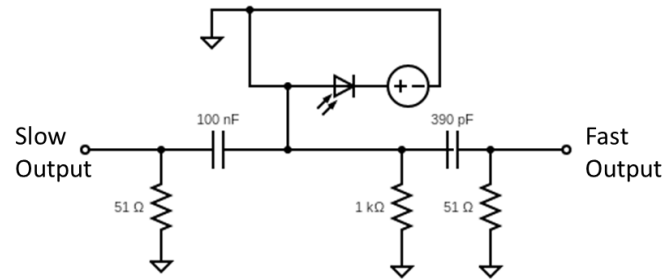


Fig. 7. Schematic diagram of the PCB circuit describing the Slow and Fast outputs.

Figure 8 describes the data acquisition system for the GAGG detectors. We have two GAGG detectors that are mounted around the atom trap during radioactive isotope experiments to detect gamma coincidences with other decay products from the trapped atoms. We also investigated the gamma coincidence timing between the two GAGG detectors which is elaborated on in Section 3.3.4. The two detectors are called GAGG1 and GAGG2 since the GAGG crystal for GAGG1 was purchased before the other one. These detectors are essentially assembled the same way, except for 2 layers of PTFE around the GAGG2 crystal compared to 3 layers around GAGG1. We were constrained by the size of the Ø3" lens tubes that the scintillators were placed in, and we had room for only a few layers of PTFE tape around the GAGG crystals along with a single layer of ESR.

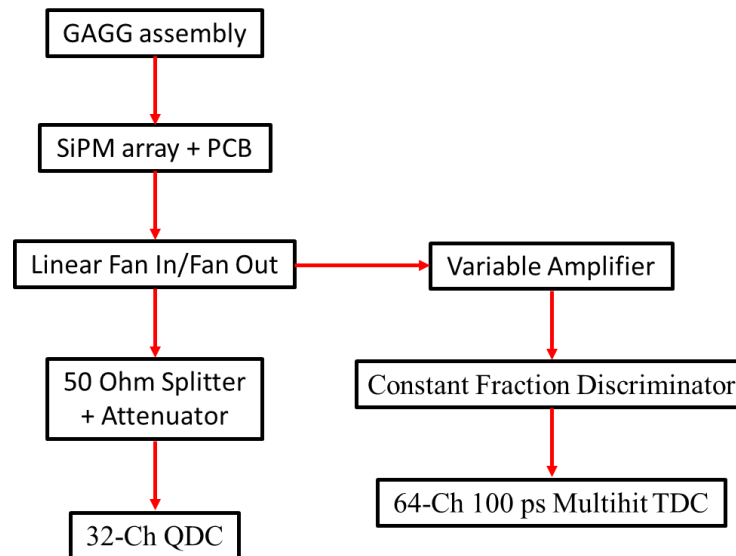


Fig. 8. Schematic diagram of the data acquisition system for the GAGG detectors.

3.3.2 Detector Calibrations

Since GAGG is a high-Z detector, it is efficient in detecting gamma-ray photopeaks. Therefore, we used a gamma-ray source, ^{60}Co traced with ^{137}Cs , to calibrate the GAGG detectors. This time, we implemented a model comprising a complementary error function describing a Compton edge and a Gaussian function describing a gamma-ray photopeak.

We fit this model on the ^{137}Cs main gamma-ray photopeak at 662 keV and the ^{60}Co photopeaks at 1173 and 1333 keV, separately. On Python, we implemented the non-linear least squares regression model to fit our model to the detector output from the QDC as well as the reduced- χ^2 test. Then, we found the channels corresponding to the means of the Gaussian distributions in our models to calibrate our detectors.

3.3.3 Optimization Studies

One of the main concerns regarding the operation of the GAGG detectors was the apparent difference in energy resolutions between the two detectors which is depicted in Fig. 9. Unlike our expectations, GAGG2 demonstrated a better energy resolution compared to GAGG1.

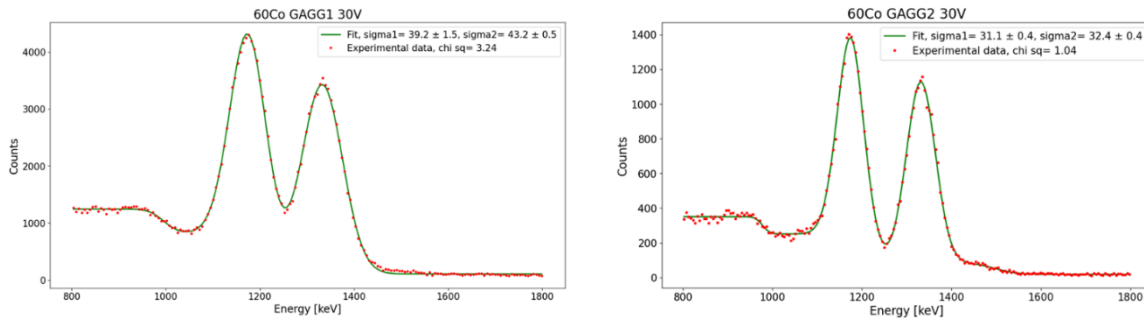


Fig. 9. The initial ^{60}Co gamma-ray spectra for the GAGG detectors biased at 30V.

The energy resolution percentages according to the initial detector calibrations are shown in Table 1, at two different photopeak energies. We noticed a $(1.7 \pm 0.5) \%$ difference in resolutions between the two detectors, with GAGG2 having better resolution. Therefore, we inspected this difference and tried various methods to improve the resolution of GAGG1.

Table 1. Energy resolutions for the GAGG detectors at different energies initially and after several modifications.

		661.7 keV	1332.5 keV	Average
Initially	GAGG1	$(9.2 \pm 0.3) \%$	$(7.6 \pm 0.3) \%$	$(8.4 \pm 0.4) \%$
	GAGG2	$(7.7 \pm 0.3) \%$	$(5.7 \pm 0.3) \%$	$(6.7 \pm 0.4) \%$
Nitrocellulose	GAGG1	$(10.2 \pm 0.3) \%$	$(8.5 \pm 0.4) \%$	$(9.3 \pm 0.5) \%$
SiPM change	GAGG1	$(10.0 \pm 0.3) \%$	$(8.1 \pm 0.4) \%$	$(9.1 \pm 0.5) \%$
Signal attenuation	GAGG1	$(9.9 \pm 0.3) \%$	$(8.1 \pm 0.4) \%$	$(9.0 \pm 0.5) \%$
	GAGG2	$(7.9 \pm 0.3) \%$	$(5.7 \pm 0.4) \%$	$(6.8 \pm 0.5) \%$
Crystal swap	GAGG1	$(7.9 \pm 0.3) \%$	$(5.8 \pm 0.4) \%$	$(6.9 \pm 0.5) \%$
	GAGG2	$(9.5 \pm 0.3) \%$	$(7.4 \pm 0.4) \%$	$(8.5 \pm 0.5) \%$

3.3.3.1 Overvoltage Optimization

Like the plastic detector, we investigated the change of energy resolution with the increasing overvoltage. Figure 10 shows the σ change (for a Gaussian distribution) at different energies with increasing bias voltage. σ values increase with \sqrt{E} and lower σ indicates better detector resolution. We observed that there is a clear difference in resolution between 26 – 27 V and the higher bias voltages. It is not straightforward to tell the impact of the overvoltage between 28 – 30 V, however, biasing the SiPMs at 30 V results in the best energy resolution. Therefore, we determined that with increasing overvoltage, the sigma values decrease, hence the energy resolution improves. It is also worth noting that we recorded the best energy resolution at 28 V for GAGG2 unlike GAGG1, and that could be due to the increasing dark current with the increasing bias voltage. This dark current could be reducing the effect of the increasing PDE. As a result, we determined that it is optimal to bias the SiPMs at ~ 5 V higher than the breakdown voltage, but not higher to prevent high dark currents.

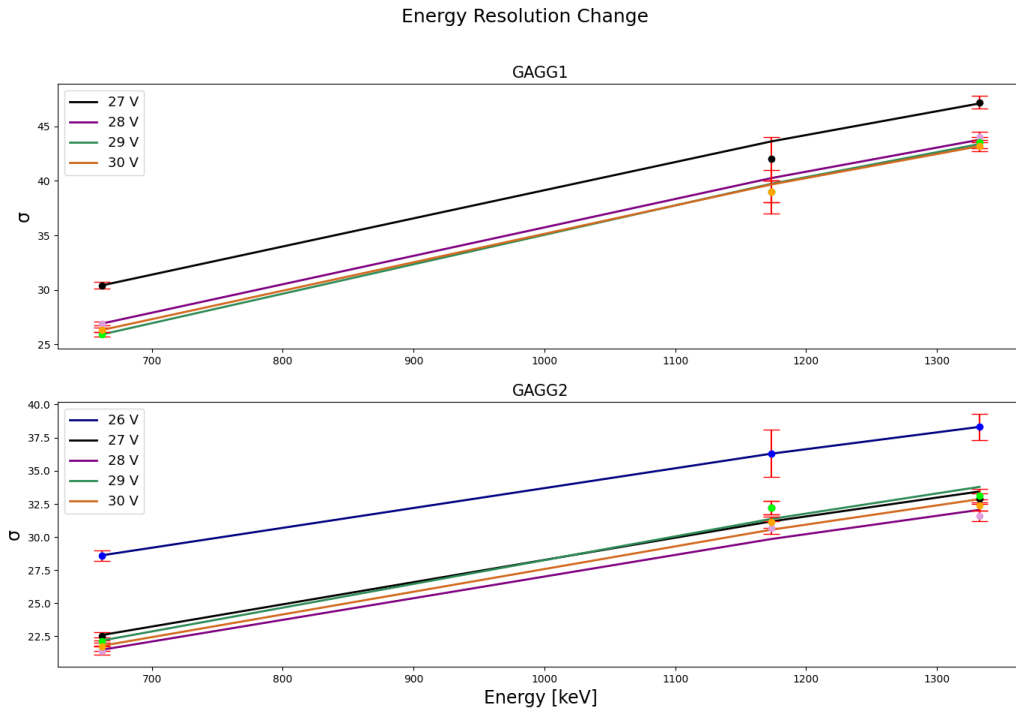


Fig. 10. Energy resolution change for the GAGG detectors with the increasing bias voltage. A square root function was fitted to the data points. σ values increase with \sqrt{E} .

3.3.3.2 Reflector Change

To increase the resolution of GAGG1, we first tried a different type of reflective material to wrap the scintillator crystal. In 2012, Janecek reported the reflection coefficient of nitrocellulose with 0.12 mm thickness to be 103% of the reflection coefficient of 4 layers of ACE Teflon tape with a thickness of 0.06 mm per layer at 440 nm [5]. Therefore, we swapped 3 layers of PTFE coating with a single layer of nitrocellulose on GAGG1. Our GAGG crystal was therefore wrapped with one layer of nitrocellulose and one layer of ESR around it. Contrary to our expectations, the average energy resolution for GAGG1 decreased from $(8.4 \pm 0.4) \%$ to $(9.3 \pm 0.5) \%$ (Table 1).

Thus, we changed the coating back to 3 layers of PTFE plus one layer of ESR and were able to restore the energy resolution.

We suspect that the main reason for this unexpected result stems from the adhesive properties of the two reflectors. The PTFE tape that we use is thinner than a single layer of nitrocellulose sheet and the thin layers stick onto themselves. However, the nitrocellulose sheets leave white dust behind and do not adhere to the surface of the scintillator as well as the PTFE tape does, preventing a tight wrapping around the scintillator. This might cause a significant amount of light loss from the small space between the nitrocellulose sheet and the scintillator surface. This problem is prevented with PTFE as the tape wraps tightly around the scintillator crystal, thus we have better energy resolution with the PTFE wrapping rather than nitrocellulose.

3.3.3.3 *Bias Current Inspection*

Another concern with GAGG1 was the high current readings while biasing the SiPMs. Since SiPMs are composed of SPADs, they are expected to have minimal current flow through their depletion region under the breakdown voltage (~ 24 V) and have an exponentially increasing current flow above it. A free charge carrier generated in the depletion region is called a dark count and the triggered discharge is the dark current. Dark current rates are usually related to changes in temperature [12]. However, the temperature in our laboratory where the detectors were situated was kept at a stable room temperature. Moreover, compared to GAGG2 which had under $30 \mu\text{A}$ current levels under the breakdown voltage, GAGG1 showed up to 0.4 mA of bias current under the breakdown voltage. Therefore, we investigated the 4 Slow output channels from the SiPM readout of GAGG1 and observed lower intensity from 2 Slow signals which sum the three 2×2 SiPM arrays attached to the lower row of the PCB. We also looked at the Fast signals of GAGG1 on the oscilloscope to see if the issue was linked to the SiPMs or the capacitors on the circuit board and observed the same difference in signal amplitudes from the same corresponding channels (Fig. 11). On the other hand, GAGG2 did not have the same issue as each 4 Slow and Fast outputs contributed almost equally.

We replicated our detector setup with a $10 \times 10 \times 10$ mm cube-shaped GAGG(Ce) crystal which we coupled with an identical PCB and investigated the bias currents for the lower row of SiPMs on GAGG1. We observed significantly higher dark currents from one of them. Thus, we replaced it with a new SensL ARRAYJ-60035-4P-PCB 6 mm SiPM. The dark current level was reduced to $60 \mu\text{A}$ under the breakdown voltage for GAGG1. Unfortunately, the average energy resolution increased to $(9.0 \pm 0.5) \%$, contrary to our expectations. We inspected the 4 Slow output signals again and attenuated them to be the same level for both detectors, however, the energy resolution did not change for either of them (Table 1).

3.3.3.4 *PCB Modification*

Next, we decided to modify our PCB since the SiPM replacement did not improve the energy resolution. Figure 11 describes the pulse signals from the 4 Fast and Slow outputs of the PCB, as obtained from GAGG1. The pulse shapes for the Slow outputs are visibly distorted, as we observed a secondary peak/bump in the decaying pulse after $1 \mu\text{s}$. We suspected that this unusual pulse shape from the Slow outputs might have been due to the Fast output arm of the PCB readout, as most readouts have a single output and do not count for fast pulses. The Fast output arm in the PCB was intended to increase the timing resolution by using a capacitor with a low value, however,

we think this causes the PCB to lose current to the Fast outputs when using the Slow output for the QDC. Therefore, we removed the 51 Ohm resistors on the Fast output arms on PCB to let all the current from the SiPM flow through the Slow outputs.

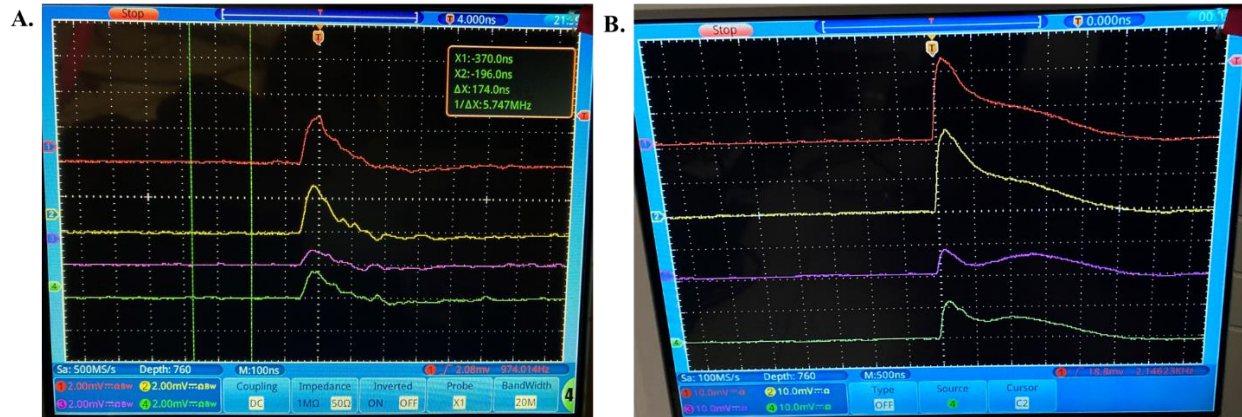


Fig. 11. SiPM readout from the PCB attached to GAGG1. Pulses from the (A) Fast and (B) Slow outputs of the PCB are shown.

We tested the modified PCB with a similar GAGG setup. We coupled the 10x10x10 mm cube-shaped GAGG(Ce) crystal with one 2x2 SensL ARRAYJ-60035-4P-PCB 6 mm SiPM on the modified PCB and observed the corresponding Slow and Fast outputs. While the shape of the pulse did not change, we observed that the ratio of the amplitudes of the slow and fast outputs decreased (from 1:6 to 1:4) since there were no resistors on the Fast outputs anymore, therefore the pulses on the fast amplitude had bigger amplitudes. We also tried to unplug the Fast outputs from the PCB and the pulse shape on the Slow outputs was still the same. We still do not know if this unusual pulse shape affects the resolution of the GAGG detectors. However, we were not able to modify the shape. Our GAGG detectors have fragile parts such as the GAGG crystal, the SiPMs which are sensitive to visible light and static discharge, and the MMCX cable connections on the PCB. Disassembling the detectors puts these parts at risk, therefore, we decided not to replace the modified PCB with the regular ones as we did not observe a clear difference.

3.3.3.5 Crystal Swap

In the end, we tried swapping the GAGG crystals to investigate the effect of the scintillator on the energy resolution since the detectors were assembled in the same way and should have exhibited similar energy resolutions. After the crystal swap, we determined average energy resolutions of $(6.9 \pm 0.5) \%$ and $(8.5 \pm 0.5) \%$ for GAGG1 and GAGG2, respectively (Fig. 12 and Table 1). This showed us that the main reason for the energy resolution differences between the two detectors was mainly due to the crystal scintillators. Indeed, the crystals were purchased from the same company at different times, and we are not aware of the modifications and improvements that the company has performed on their crystals between the two purchases. However, we can deduce from these results that the intrinsic crystal properties highly affect the energy resolution of the scintillation detectors.

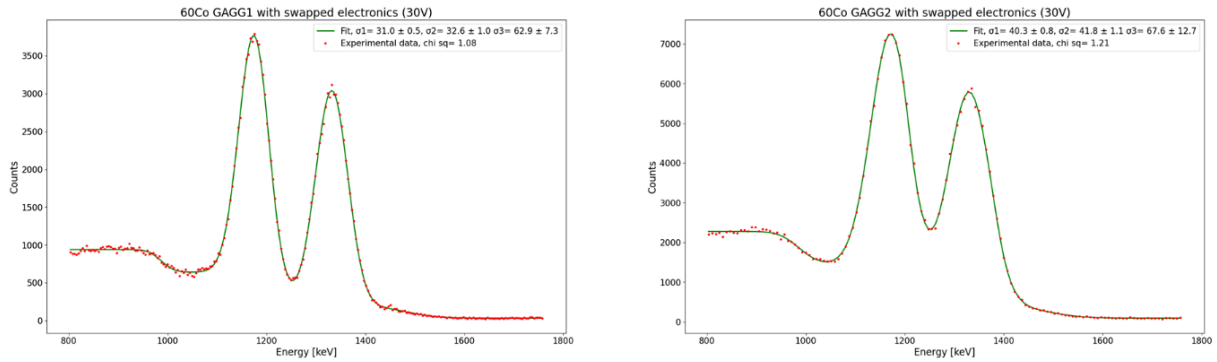


Fig. 12. ^{60}Co gamma-ray spectra for the GAGG detectors biased at 30V, after the GAGG crystals were swapped.

3.3.4 Coincidence Timing Resolution

The timing resolution is related to the number of scintillation photons of the fast component of the scintillation events, or the density of photoelectrons generated in the detector at the detection threshold [3,13]. It depends on the rise and decay time of the pulses as well as the readout electronics [3]. SiPMs are known to provide high timing resolution when coupled with scintillators [14]. Therefore, we investigated the coincidence timing resolution between the GAGG detectors.

By using the timing information for the two GAGG detectors, we isolated the events during which both detectors were able to detect photons and constructed a coincidence timing histogram. Figure 13 describes the gamma-ray coincidences between the GAGG detectors for the relative timing of $t_{\text{GAGG1}} - t_{\text{GAGG2}}$. The specific timing ntuples that were extracted from ROOT to access the timing information were: `TDC_BGO_1_LE[0]` and `TDC_BGO_2_LE[0]`. After fitting a normal distribution to the coincidence timing histogram, we determined a coincidence timing resolution of 6.1 ± 0.5 ns for the two GAGG detectors.

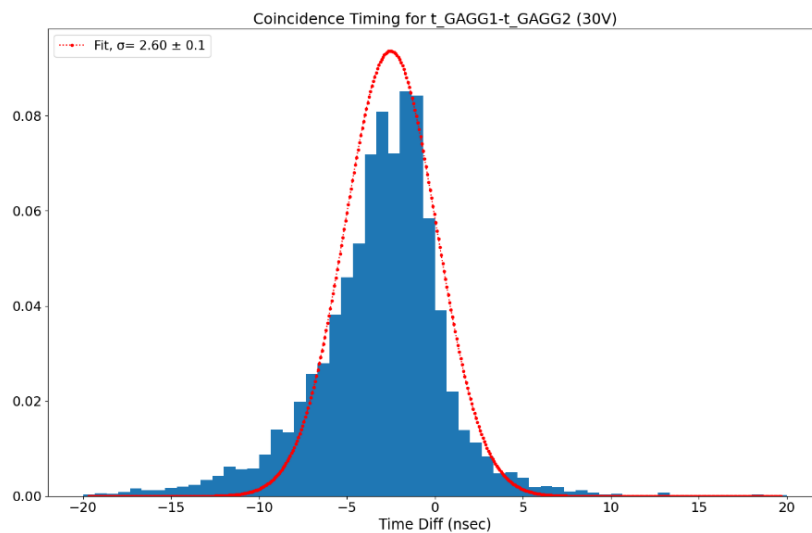


Fig. 13. Coincidence timing resolution between the GAGG detectors.

We also plotted an energy graph for the coincidence timing, to be able to see the location of the density of scintillation photons on the energy spectrum. The specific energy ntuples that were extracted from ROOT were QDC_BGO_1 and QDC_BGO_2. Figure 14 reveals that for the coincidence timing, a high density of photons was emitted around the two main known gamma-ray photopeaks of ^{60}Co at 1173 and 1333 keV. However, we also noticed a lot of events below those energies, especially below 500 keV. This allows us to determine that isolating events for the known gamma-ray photopeaks might be crucial for eliminating background noise while plotting the timing histograms and investigating the timing resolutions.

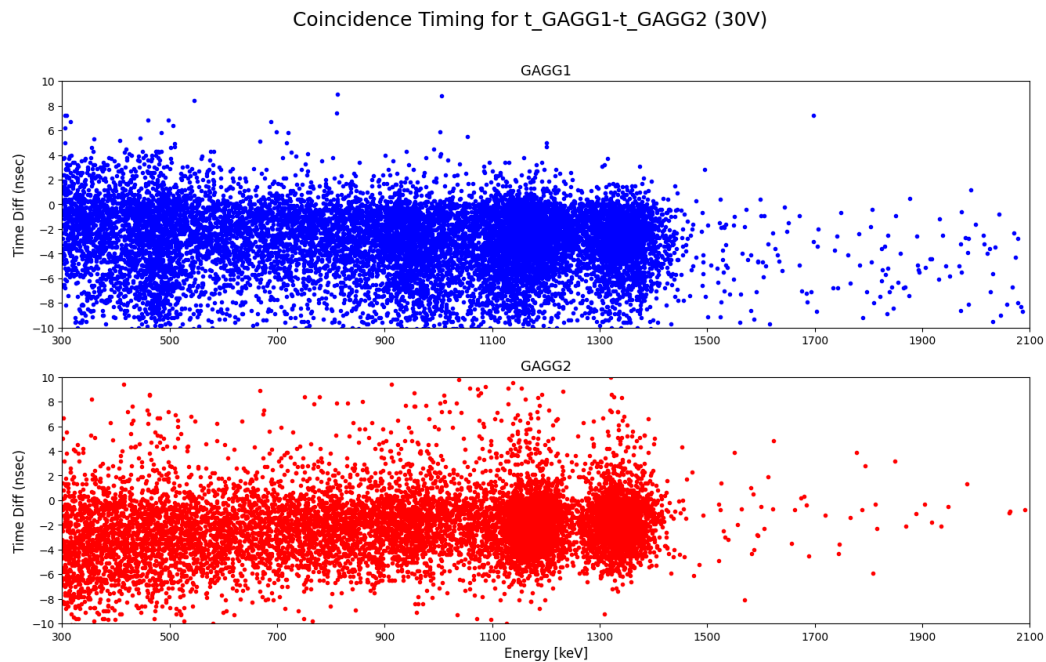


Fig. 14. Energy and time distribution of the coincidence events between the two GAGG detectors. The densest areas seen in circles in the middle of the plots for both detectors correspond to the main gamma-ray photopeaks of ^{60}Co at 1173 and 1333 keV.

4 Future Perspectives

We conducted a test experiment with a radioactive potassium isotope, ^{45}K , as obtained from the beamline of the cyclotron at TRIUMF at the end of August. We are analyzing the data collected during this 24-hour-long experiment. I have been observing the gamma-ray spectra obtained by the GAGG detectors. I am mainly observing the gamma-ion coincidences as occurred during the ^{45}K experiments. I plan to continue this analysis. Furthermore, we have been developing a 3D housing model on COMSOL and TinkerCAD for our newest plastic scintillators attached to a waveguide that will be inserted inside the atom trap in our laboratory. We also plan to conduct test runs with these new plastic scintillators with and without a waveguide and compare the results. I plan to work on testing the new electronic parts we acquired such as the new HV and SiPM evaluation boards and assembling the plastic scintillation detectors along with the housing model we have been building.

5 Conclusion

We performed calibration and optimization studies for a plastic and two GAGG detectors for achieving high precision measurements required for the time-reversal symmetry violation search in trapped atoms. We showed the use of a differentiation method to estimate the location of Compton edges for gamma-ray emissions for calibrating an organic scintillator. GEANT4 simulations convolved with Gaussian distributions were used to assess the energy resolution change at different bias voltages. We found that the energy resolution for the organic scintillation detector increases with the increasing bias voltage due to an increase in photon detection efficiency. We determined an energy resolution of 10-11% for internal conversion electrons around 1 MeV for the plastic scintillator. Moreover, nitrocellulose was found to be ineffective as a reflector material to wrap the scintillators compared to 2-3 layers of PTFE due to its non-adhesive nature on the scintillator crystal surface. We also investigated the differences in energy resolution between two “identical” inorganic GAGG detectors. A SiPM change, pulse signal attenuation and PCB modification failed to improve the energy resolution and we could trace the main reason for the lower resolution of one of the GAGG detectors after swapping the crystals. We determined that the slightly different crystal compositions highly affect the energy resolution of the scintillation detectors. The average energy resolutions for GAGG detectors were determined as 8.9% and 6.9% at 662 and 1333 keV gamma-ray photopeaks, respectively. Coincidence timing resolution between the GAGG detectors was also investigated and determined as 6.1 ± 0.5 ns.

References

- [1] <https://trinat.triumf.ca/>
- [2] Knoll, Glenn F. *Radiation detection and measurement*. John Wiley & Sons, 2010.
- [3] Yanagida, Takayuki. "Inorganic scintillating materials and scintillation detectors." *Proceedings of the Japan Academy, Series B* 94.2 (2018): 75-97.
- [4] Bill Collum. “11 - Radiometric Instruments.” *Nuclear Facilities*, Elsevier Ltd, 2017, pp. 349–68, <https://doi.org/10.1016/B978-0-08-101938-2.00011-8>.
- [5] Janecek, M. “Reflectivity Spectra for Commonly Used Reflectors.” *IEEE Transactions on Nuclear Science*, vol. 59, no. 3, 2012, pp. 490–97, <https://doi.org/10.1109/TNS.2012.2183385>.
- [6] <https://www.onsemi.com/pub/Collateral/AND9770-D.PDF>
- [7] Genat, Jean-Francois, et al. "Signal processing for picosecond resolution timing measurements." *Nuclear Instruments and Methods in Physics Research Section A: Accelerators, Spectrometers, Detectors and Associated Equipment* 607.2 (2009): 387-393.
- [8] Jolivet, P. L., and N. Rouze. "Compton scattering, the electron mass, and relativity: A laboratory experiment." *American Journal of Physics* 62.3 (1994): 266-271.
- [9] Safari, M. J., F. Abbasi Davani, and H. Afarideh. "Differentiation method for localization of Compton edge in organic scintillation detectors." arXiv preprint arXiv:1610.09185 (2016).

[10] M.E. Rose: "Theory of Internal Conversion", in: Alpha-, Beta- and Gamma-Ray Spectroscopy, ed. by Kai Siegbahn, North-Holland Publishing, Amsterdam (1966), Vol. 2

[11] <https://www.epic-crystal.com/oxide-scintillators/gagg-ce-scintillator.html>

[12] Thiessen, Jonathan D., et al. "Performance evaluation of SensL SiPM arrays for high-resolution PET." *2013 IEEE Nuclear Science Symposium and Medical Imaging Conference (2013 NSS/MIC)*. IEEE, 2013.

[13] Lecoq, P., et al. "Factors influencing time resolution of scintillators and ways to improve them." *IEEE Transactions on Nuclear Science* 57.5 (2010): 2411-2416.

[14] Radun, Filip. Time resolution in scintillator-based detectors for positron emission tomography (Doctoral Dissertation). No. CERN-STUDENTS-Note-2019-010. (2019).